International Journal of Nanomedicine

Dovepress

open access to scientific and medical research

Open Access Full Text Article

ORIGINAL RESEARCH

Iron-Based Nanovehicle Delivering Fin56 for Hyperthermia-Boosted Ferroptosis Therapy Against Osteosarcoma

Yiran Zhang[1–4,*], Qingcheng Song[2,3,*], Yueyao Zhang[2,3,*], Jiheng Xiao[5], Xiangtian Deng[6], Xin Xing[2,3], Hongzhi Hu[5], Yingze Zhang[1–3]

[1]School of Medicine, Nankai University, Tianjin, 300071, People's Republic of China; [2]Department of Orthopaedic Surgery, Third Hospital of Hebei Medical University, Shijiazhuang, Hebei, 050051, People's Republic of China; [3]NHC Key Laboratory of Intelligent Orthopaedic Equipment, Third Hospital of Hebei Medical University, Shijiazhuang, Hebei, People's Republic of China; [4]HeBei Ex&Invivo Biotechnology Co. Ltd, Shijiazhuang, Hebei, 050051, People's Republic of China; [5]Department of Orthopaedics, Union Hospital, Tongji Medical College, Huazhong University of Science and Technology, Wuhan, 430022, People's Republic of China; [6]Orthopaedics Research Institute, Department of Orthopaedics, West China Hospital, Sichuan University, Chengdu, Sichuan, 610041, People's Republic of China

*These authors contributed equally to this work

Correspondence: Yingze Zhang; Hongzhi Hu, Email yzling_liu@163.com; 13720105746@163.com

Background: Although systemic chemotherapy is a standard approach for osteosarcoma (OS) treatment, its efficacy is limited by the inherent or acquired resistance to apoptosis of tumor cells. Ferroptosis is considered as an effective strategy capable of stimulating alternative pathways of cancer cell demise. The purpose of this study is to develop a novel strategy boosting ferroptotic cascade for synergistic cancer therapy.

Methods and Results: A novel nanovehicle composed of arginine-glycine-aspartate (RGD) modified mesoporous silica-coated iron oxide loading Fin56 was rationally prepared (FSR-Fin56). With the RGD-mediated targeting affinity, FSR-Fin56 could achieve selective accumulation and accurate delivery of cargos into cancer cells. Upon exposure to NIR light, the nanovehicle could generate localized hyperthermia and disintegrate to liberate the therapeutic payload. The released Fin56 triggered the degradation of GPX4, while Fe^{3+} depleted the intracellular GSH pool, producing Fe^{2+} as a Fenton agent. The local rise in temperature, in conjunction with Fe^{2+}-mediated Fenton reaction, led to a rapid and significant accumulation of ROS, culminating in LPOs and ferroptotic death. The outstanding therapeutic efficacy and safety of the nanovehicle were validated both in vitro and in vivo.

Conclusion: The Fin56-loaded FSR nanovehicle could effectively disturb the redox balance in cancer cells. Coupled with NIR laser irradiation, the cooperative CDT and PTT achieved a boosted ferroptosis-inducing therapy. Taken together, this study offers a compelling strategy for cancer treatment, particularly for ferroptosis-sensitive tumors like osteosarcoma.

Keywords: chemodynamic therapy, photothermal therapy, Fenton reaction, Fin56, ferroptosis

Introduction

Osteosarcoma (OS), the most common primary bone malignancy with a high mortality rate in young individuals,[1] remains a therapeutic challenge. Although systemic chemotherapy (pre- and postoperative) is a standard approach for OS treatment, its efficacy is limited by the inherent or acquired resistance to apoptosis of tumor cells.[2] Hence, there is a pressing need for novel strategies capable of stimulating alternative pathways of cellular demise, in order to overcome the limitations of current systemic agents that induce apoptosis.

Ferroptosis, as a newly discovered type of non-apoptotic cell death, was characterized by distinct morphological and biochemical features.[3] As the intersection of this unique cell death process, suppression of glutathione peroxidase 4 (GPX4) activity leads to the disruption of intracellular reactive oxygen species (ROS) scavenging and generation equilibrium.[4] Subsequently, the excessive accumulation of ROS induces lipid peroxidation of the cell membrane and

Received: 19 September 2023
Accepted: 19 December 2023
Published: 4 January 2024

Graphical Abstract

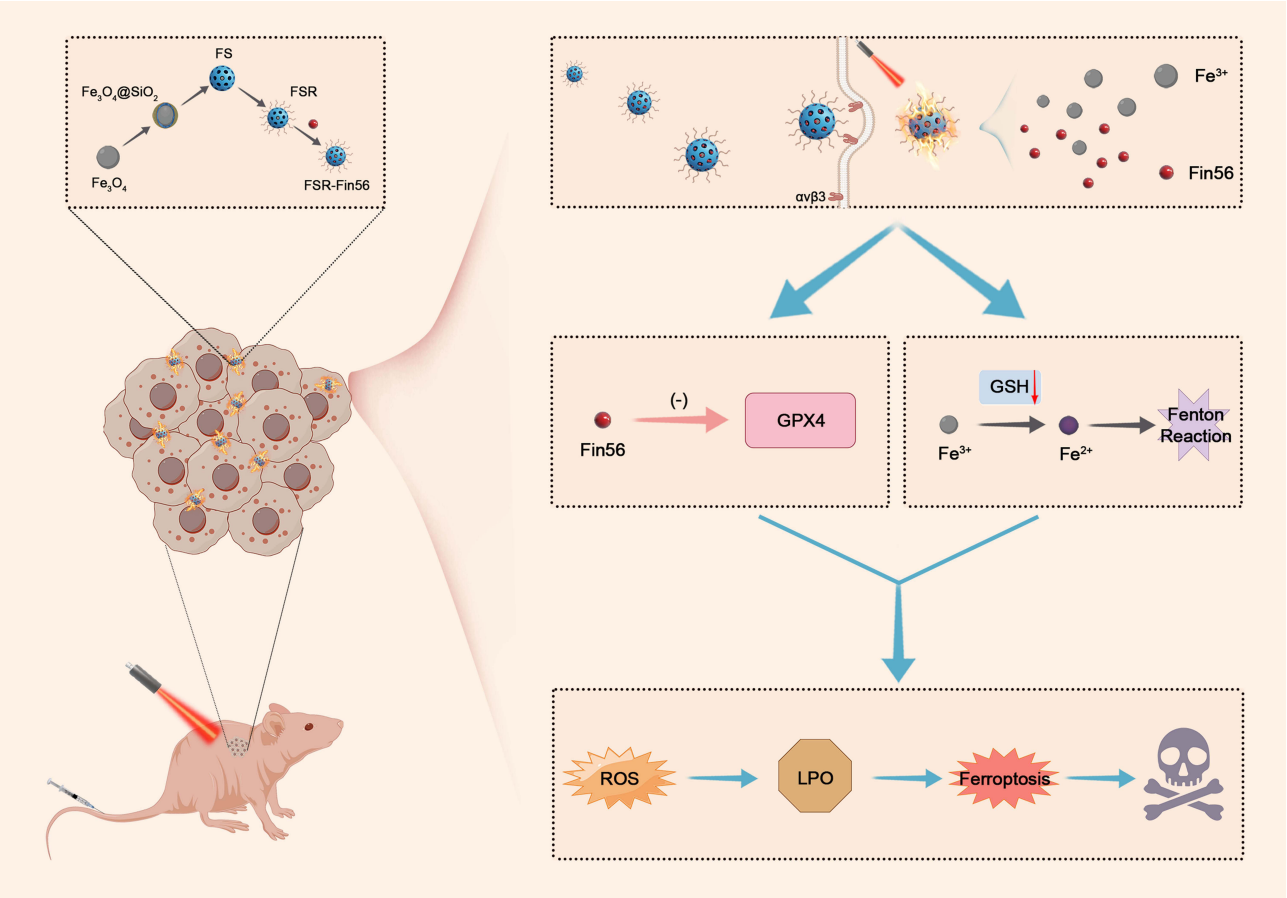

ultimately triggers the ferroptotic cascade.[5,6] Meanwhile, being an iron-dependent form of cell death, ferroptosis is closely linked to intracellular Fe^{2+}/Fe^{3+} levels,[7] which mediate the Fenton reaction catalyzing intracellular hydrogen peroxide (H_2O_2) and promote the accumulation of both ROS and lipid peroxides (LPOs).[8,9] Thus, ferroptosis-inducing therapy is anticipated to overcome the drawbacks of traditional apoptosis-mediated therapeutics. Several studies have provided evidence that ferroptosis could represent a promising therapeutic strategy for OS.[10–12] Recently, an expanding array of iron-based nanomaterials have been developed to induce ferroptosis in cancer therapies.[13–15] Nevertheless, these nanoparticles alone exhibit inadequate catalytic efficiency and encounter a redox homeostasis that counteracts the accumulation of ROS, thereby hindering their ability to induce lethal ferroptosis in tumor cells. In that case, the exploration of combined strategy for enhanced ferroptosis-inducing therapy with redox disruption ability and higher catalytic efficiency has gained tremendous momentum.

Fin56, a newly discovered type 3 inducer, has been shown to trigger ferroptosis by directly promoting the degradation of GPX4.[16] Studies have provided evidence that Fin56 can activate ferroptosis in cancer cells and exhibit potent anti-tumor effects.[17,18] However, due to the evolved self-repair mechanism by tumor cells, the elevated intracellular glutathione (GSH) levels,[19] which can promote GPX4 activity as an antioxidant molecule, compromises the anti-tumor effects of using GPX4 inhibitors such as Fin56 alone. Therefore, a combination therapy involving GSH depletion is necessary to thoroughly disrupt the redox homeostasis of cancer cells.

Iron oxide (Fe_3O_4) nanoparticles have recently garnered considerable attention for oncological applications due to their biocompatible nature, low toxicity and photothermal properties.[20,21] The released Fe^{3+} ions from Fe_3O_4 can deplete intracellular

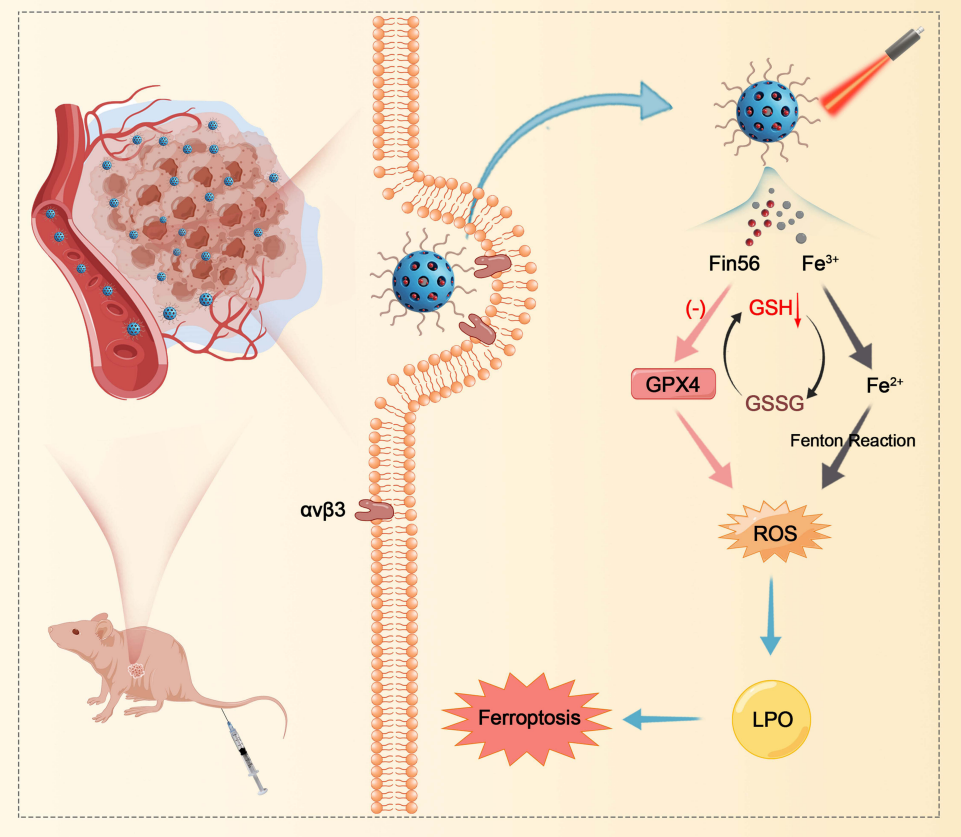

Scheme 1 Application of FSR-Fin56 in the hyperthermia-boosted ferroptosis therapy.

GSH, while the resulting Fe^{2+} mediates the local Fenton reaction, leading to a rapid increase of intratumoral ROS levels and induction of ferroptosis.[22,23] Additionally, due to its excellent photothermal effect, Fe_3O_4 nanoparticles can be used in combination with photothermal therapy (PTT),[24,25] where increased temperature can enhance the electrochemical catalytic efficiency of the Fenton reaction, resulting in a synergistic anti-tumor effect.[26] Therefore, the combined use of Fin56 and Fe_3O_4 nanoparticles can completely disrupt the redox balance of tumor cells and improve the catalytic efficiency of the ROS generating reaction, leading to an enhanced Ferroptosis-inducing modality for anti-tumor strategy.

In this study, we developed a versatile core-shell nanovehicle comprising Fe_3O_4 core and mesoporous silica coating functionalized with arginine-glycine-aspartate (RGD) peptide and loaded with Fin56, termed FSR-Fin56. As is known, RGD peptide exhibits interaction with αvβ3 and αvβ5 integrin receptors, which are broadly distributed among diverse cancer cells.[27] Our study specifically targets OS cells, where these integrin receptors are prominently expressed[28] and could be utilized by the RGD-functionalized nanovehicle fulfilling targeted delivery. As depicted in Scheme 1, FSR-Fin56 could selectively accumulate in OS cells by virtue of the RGD-mediated targeting affinity. Upon exposure to NIR light, the nanovehicle could generate localized hyperthermia and disintegrate to liberate the therapeutic payload. The released Fin56 triggered the degradation of GPX4, while Fe^{3+} depleted the intracellular GSH pool, producing Fe^{2+} as a Fenton agent. The local rise in temperature, in conjunction with Fe^{2+}-mediated Fenton reaction, led to a rapid and significant accumulation of ROS, culminating in LPOs and ferroptotic death. As a consequence, tumor suppression was achieved via FSR-Fin56-mediated hyperthermia and ferroptosis. This research extends the scope of Fin56 applications to OS and offers a promising hyperthermia-boosted ferroptosis strategy, which synergistically enhances anticancer efficacy by exploiting targeted delivery and amplified ferroptosis.

Materials and Methods

Materials

Iron chloride hexahydrate ($FeCl_3 \cdot 6H_2O$), tetramethyl-benzidine (TMB), tetraethylorthosilicate (TEOS, 99.99%), sodium acetate anhydrous and ethylene glycol (EG) were obtained from Aladdin (Shanghai, China). Fin56 and 2',7'-

dichlorodihydrofluorescein diacetate (DCFH-DA) were purchased from Cayman (Cayman Chemicals, MI, USA). RGD peptide (Arg-Gly-Asp, purity >97%) was purchased from GL Bio-Chem Co., Ltd (Shanghai, China). All remaining reagents and chemicals were acquired at the highest available purity and used without additional purification.

Synthesis of Fe_3O_4

The synthesis of Fe_3O_4 nanoparticles followed a slightly modified version of previously reported methods.[29] Briefly, 2.7 g of $FeCl_3 \cdot 6H_2O$ and 3.6 g of sodium acetate were dissolved in 50 mL of ethylene glycol and stirred until the solution became clear. This mixture was then transferred to an autoclave and heated to 200°C for 12 hours. The resulting product was collected through centrifugation, washed with pure water and ethanol, and subsequently dried. The obtained product was further ground into powder to yield Fe_3O_4 NPs.

Synthesis of Fe_3O_4@mSiO_2(FS)

Fe_3O_4@SiO_2 NPs were synthesized using a modified Stöber sol-gel method.[30] Initially, 500 mg of Fe_3O_4 NPs were dispersed in 25 mL of 0.1M HCl solution through sonication and subsequent washing. A mixture of water, ethanol, and ammonia aqueous solution (14 wt%) was prepared in a volume ratio of 10:40:1. The NPs were dispersed in this mixture using ultrasonic agitation, and then 15 mg of TEOS was dropwise added with continuous stirring for 12 hours. The resulting Fe_3O_4@SiO_2 NPs were obtained through centrifugation and washed three times with pure water and ethanol. To introduce the mesoporous structure, a mixture of HCl and water (4:1 v/v) was used to etch the NPs at room temperature for 50 seconds. Afterwards, the NPs were collected, washed, dried, and ground into powder to yield Fe_3O_4@mSiO_2 nanoparticles.

Synthesis of Fe_3O_4@mSiO_2@RGD(FSR)

To synthesize Fe_3O_4@mSiO_2@RGD, the amine-functionalized Fe_3O_4@mSiO_2 (FS-NH_2) nanoparticles were prepared with some adjustments to a previously reported method.[29] Initially, the obtained FS nanoparticles were dispersed and reacted with APTES in ethanol under stirring at 50°C for 12 hours. After removing excess APTES through magnetic separation, RGD peptide was conjugated to the amine-functionalized FS nanoparticles with a 10^2-fold molar excess compared to the nanoparticles, using EDC and NHS as coupling agents.[31] Following 12 hours of stirring at room temperature, the FSR nanoparticles were obtained through centrifugation and subsequently washed twice with distilled water.

Characterizations

Transmission electron microscopy (TEM) images were captured using a Hitachi HT7800 electron microscope. Scanning electron microscopy (SEM) images and corresponding energy-dispersive spectroscopy (EDS) mapping analyses were performed using a Hitachi Regulus 8100 electron microscope. Size distribution and zeta potential were assessed via a Malvern Zeta sizer Nano ZS90 instrument. Fourier transform infrared (FTIR) spectra were recorded on a Thermo Nicolet iS50 FTIR spectrometer. UV-vis absorption spectra were obtained using a spectrophotometer (UV-3600, Shimadzu, Japan). The sample's Brunauer–Emmett–Teller (BET) specific surface area was determined using a JW-BK132 F instrument.

Photothermal Properties

To assess the in vitro photothermal capabilities of FSR NPs, real-time temperature changes were monitored and recorded using an infrared thermal imaging camera (Testo 865) at predefined intervals. To explore the concentration and time-dependent photothermal behavior, varying concentrations of FSR NPs in PBS were subjected to 808 nm laser irradiation (1.0 W cm^{-2}) for 10 minutes. Additionally, to examine the influence of laser power density, 100 μg mL^{-1} samples were exposed to different power densities (0.5, 1.0, 1.5, and 2.0 W cm^{-2}) for 10 minutes. For evaluating photothermal stability, FSR NPs underwent irradiation for 10 minutes, followed by cooling to room temperature before the subsequent cycle. The temperature changes during five consecutive irradiation ON/OFF cycles were recorded to determine photothermal stability.

Fenton Effect

To measure hydroxyl radicals generated in the Fenton reaction, 4,4'-Diamino-3,3',5,5'-tetramethylbiphenyl (TMB) was employed. The test samples were categorized as follows: (i) FSR NPs at pH 7.4; (ii) FSR NPs at pH 5.0; (iii) FSR NPs plus H_2O_2 at pH 7.4; (iv) FSR NPs plus H_2O_2 at pH 5.0; (v) FSR NPs plus H_2O_2 and GSH (10mM) at pH 7.4; (vi) FSR NPs plus H_2O_2 and GSH (10mM) at pH 5.0. All experiments were conducted at room temperature (25°C) with a concentration of 50 ug/mL for FSR NPs. TMB was dissolved in DMSO and then diluted into a 500 μM solution using pure water before adding to FSR NPs. TMB solution was mixed with FSR NPs with or without H_2O_2 treatment, and the absorbance was recorded at pH 5.0 or pH 7.4. For fluorescence experiments detecting OH· generation, hydroxyphenyl fluorescein (HPF) was employed as the fluorescent probe. It was added to the systems mentioned above with a final concentration of 10 μM. Following a 1-hour incubation, the solutions were subjected to photoexcitation at 490 nm and the fluorescence intensity was recorded. Furthermore, the influence of temperature in the Fenton reaction was assessed. The experimental groups included: (i) PBS under 25°C; (ii) PBS plus H_2O_2 and GSH under 25°C; (iii) FSR plus H_2O_2 and GSH under 25°C; (iv) FSR plus H_2O_2 and GSH under 50°C. The absorbance was measured accordingly.

In vitro Drug Loading and Release

For detection of the loading efficiency, different ratios of FSR and Fin56 (8:1, 4:1, 2:1, 1:1, 0.5:1 w/w) were incubated in PBS (pH=7.4) under continuous stirring for 12 hours at room temperature. The resulting FSR-Fin56 NPs were obtained through centrifugation, washed with deionized water, and stored for later use. The supernatant was collected for UV-vis spectrum analyses to measure loading efficiency.

For assessing the pH and irradiation-triggered Fin56 release, FSR-Fin56 was incubated in PBS at two pH levels (5.0 and 7.4) at 37°C. This was done both in the presence and absence of an 808 nm laser (1 W/cm^2). At specified time intervals, the mixture was centrifuged, and the supernatant was collected. The residual solution was replenished with corresponding PBS. The concentration of released Fin56 was determined by measuring the absorbance of the supernatant at 300 nm using an UV-vis spectroscopy.

Cellular Assays

Cell Lines and Culture

The human osteosarcoma cell line (MNNG/HOS) and human bone marrow stromal cells (BMSCs) were procured from the Cell Bank at the Shanghai Institute of Biochemistry and Cell Biology, Chinese Academy of Sciences. MNNG/HOS cells were cultured in α-modified essential medium (α-MEM) supplemented with 10% fetal bovine serum (FBS) and 1% antibiotics. Bone marrow stromal cells were cultured in DMEM/F12 with 15% FBS and 1% penicillin-streptomycin. Incubation was carried out at 37°C with 5% CO_2.

Cellular Uptake

MNNG/HOS cells were cultured in 6-well plates with 8×10^4 cells per well and incubated for 12 hours. Afterward, the cells were treated with ICG@FS or ICG@FSR NPs (at a concentration of 20 ug mL^{-1}) for 4 hours. Following treatment, the cells were washed thrice with PBS and subsequently stained with Hoechst 33,342 for 15 minutes. Fluorescence microscopy (Olympus Corporation, Tokyo, Japan) was then used to observe and document the cells.

Cell TEM

The treated cells were fixed with 2.5% glutaraldehyde for 4 hours, washed with 1/15 M phosphate buffer, and then treated with 1% OsO_4 in 0.1 M Sorenson's buffer for 2 hours. After dehydration through an acetone series, the cells were embedded in Lx-112 and Embed-812. Thin sections were cut using a Leica EM UC7 ultramicrotome, stained with 1% uranyl acetate and 0.4% lead citrate, and examined under a HT7800 electron microscope.

Cell Viability Assay

Cell viability was assessed using the cell counting kit-8 (CCK-8) assay, with the data representing the mean of three parallel measurements. In brief, cells were seeded in 96-well plates at a density of 5×10^3 cells per well and incubated for

12 hours. Subsequently, the medium was replaced with fresh medium containing varying concentrations of treatment NPs (0.25, 0.5, 1, 1.5, 2, 2.5 μM). After 4 hours of incubation, specific groups were exposed to 808 nm irradiation (1 W/cm^2, 5 minutes). Following an additional 20-hour incubation, the supernatant was removed, and the cells were washed twice with PBS. Next, the cells were co-cultured with 200 μL of fresh medium containing CCK-8 operating solution for 2 hours in the dark. Cell viability was determined by measuring the absorbance at 450 nm.

Live/Dead Cells Staining

Cells were seeded in 12-well plates at a density of 2×10^4 cells per well and cultured for 12 hours. Following the aforementioned treatments, the cells were incubated for an additional 20 hours and then provided with fresh medium. Subsequently, Calcein-AM (10 μg/mL) and PI (10 μg/mL) were introduced into the medium and incubated for 20 minutes. After being washed twice with PBS, the cells were examined and visualized using a fluorescence microscopy.

Intracellular Oxidation Levels

Cells were cultured in 6-well plates with a density of 5×10^5 cells per well and incubated for 12 hours. After applying various treatments, the cells underwent the following procedure to assess intracellular oxidation levels.

For intracellular GSH detection, MNNG/HOS cells were suspended in 200 μL of PBS per well and disrupted using ultrasonication. The disrupted cells were mixed with GSH probe precipitant in a 1:1 ratio (v/v) and then centrifuged at 3500 rpm for 10 minutes. The supernatant's absorbance at 405 nm was measured, and GSH levels were determined using a GSH assay kit as per its instructions. Intracellular lipid peroxidation (LPO) was assessed by measuring MDA levels using an LPO MDA assay kit (S0131S, Beyotime, Shanghai, China) following established methods.[32] For visualizing cellular ROS, the fluorescent probe 2',7'-dichlorodihydrofluorescein diacetate (DCFH-DA) was employed. DCFH-DA emits green fluorescence upon reacting with ROS. The treated cells were rinsed, stained with DCFH-DA (10 μM) for 20 minutes, and then washed with PBS twice. Subsequently, the cells were observed and imaged using a fluorescence microscope.

Hemolysis Assay

Red blood cells (RBCs) were isolated from 1000 μL anticoagulated whole blood samples through centrifugation (4°C, 8000 rpm, 5 min), followed by three washes and dilution with 2000 μL PBS. Subsequently, 300 μL of the diluted RBC suspensions were mixed with 1200 μL of ultrapure water as a positive control, PBS as a negative control, and varying concentrations of FSR NPs (5–200 μg/mL). The mixtures were then incubated on a shaker at 37°C for 2 hours and centrifuged for 5 minutes (4°C, 8000 rpm). The absorbance at 541 nm of the supernatant was measured using a UV-vis spectrophotometer, and the hemolysis percentage was calculated as follows: Hemolysis percentage = (A sample – A (-)) / (A (+) – A (-)) × 100%. Here, A sample, A (+), and A (-) represent the absorbance of the sample, negative control, and positive control, respectively.

Animal Studies

Tumor Models

Female athymic BALB/c nude mice, 6 weeks old, were procured from Beijing HFK Bioscience Co. Ltd. All animal experiments were approved by Experimental Animal Ethics Committee of HeBei Ex&Invivo Biotechnology Co. Ltd (protocol registry number: SY2020-01). The animal-related procedures were performed in accordance with the Animal Research: Reporting of In vivo Experiments guidelines. To establish subcutaneous xenograft models, MNNG/HOS cells (2×10^{-6}) suspended in 150 μL of cold PBS were subcutaneously injected into the right flank of nude mice. Tumor dimensions were measured, with length representing the longest dimension and width representing the shortest. Tumor volume was calculated using the formula: Tumor volume = 0.5 × length × (width)^2. For in vivo therapy experiments, mice were used when tumors reached approximately 100 mm^3 in volume.

In vivo Fluorescence and Photothermal Imaging

For in vivo fluorescence imaging, mice with tumors received an injection of 150 μL of ICG-labeled FSR NPs (1 mg/L) through the tail vein. Imaging was conducted at predetermined time points (0 h, 2 h, 4 h, 8 h, 12 h, and 24 h) after

injection, with anesthesia administered to the mice (n=3) prior to imaging. The imaging process utilized a small animal imaging system (PerkinElmer, Waltham, USA). Subsequent to the final time point, the mice were euthanized, and tumor tissues as well as major organs were collected for further imaging. For in vivo photothermal imaging, an injection of 150 μL of either PBS or FSR NPs (1 mg/L) was performed. At 12 h post-injection, the tumor regions received irradiation from an 808 nm laser (1.0 W/cm^2) for 6 minutes. The changes in temperature within the tumor region were recorded using an infrared thermal imaging camera (Testo 865) at one-minute intervals.

In vivo Antitumor Effect and Biosafety

Once the tumor sizes reached approximately 100 mm^3, the mice were randomly assigned to five groups (each consisting of 5 mice) and subjected to the following treatments: (1) PBS + NIR; (2) Fin56 + NIR; (3) FSR-Fin56; and (4) FSR-Fin56 + NIR. At day 0, 4, 8, and 12, 150 μL of various treatment agents were injected into the tail vein of the tumor-bearing mice. The dose of Fin56 at each injection was 7 mg kg^{-1} and the pH of PBS was 7.4. At 12 hours post-injection, the tumor site underwent 808 nm NIR laser irradiation (1.0 W/cm^2, 6 minutes). Throughout the therapy period, the tumor volume and body weight of the mice were monitored every alternate day. After 16 days of treatment, blood samples were collected, and the tumors along with major organs (heart, liver, lung, spleen, and kidney) were fixed in 4% paraformaldehyde for subsequent experiments. Serum samples were obtained by centrifugation for hepatic and renal function analyses. The main organs and tumor tissues were sectioned for H&E (Solarbio, G1121) and immunofluorescence staining. Antibodies utilized included Ki67 (Affinity, AF0198, 1:200) and GPX4 (Huabio, ET1706-45, 1:100). Fluorescence-conjugated secondary antibodies included donkey anti-rabbit IgG (H + L) FITC (Alexa Fluor 488) (Invitrogen, A-212206; 1:500) and donkey anti-rabbit IgG (H + L) TRITC (Invitrogen, A16026; 1:500).

Statistical Analysis

Data were expressed as mean ± standard deviation (SD) and each experiment was repeated three times. Statistical significance was assessed using Student's *t*-test, one-way and two-way analysis of variance (ANOVA). A significance level of $P < 0.05$ was considered statistically significant (* $P < 0.05$, ** $P < 0.01$, *** $P < 0.001$, **** $P < 0.0001$).

Results and Discussion

Synthesis and Characterization of FSR-Fin56

Figure 1A illustrated the schematic representation of the synthesis process of Fe_3O_4@mSiO_2@RGD-Fin56, denoted as FSR-Fin56. The fabrication of Fe_3O_4@mSiO_2 (FS) nanoparticles followed a previously reported method with subtle modifications.[29] Initially, monodispersed Fe_3O_4 nanoparticles were synthesized using the solvothermal method and subsequently coated with a silica layer through the sol-gel process.[30] The resulting core-shell nanoparticles were further subjected to acid etching, which induced the formation of a highly desirable mesoporous structure on the surface and then functionalized with RGD peptide, yielding Fe_3O_4@mSiO_2@RGD (FSR) NPs. Finally, Fin56, the therapeutic agent, was loaded onto the FSR NPs to create the multifunctional therapeutic nanovehicle termed FSR-Fin56.

The TEM image presented in Figure 1B revealed a uniform and spherical morphology of the FS NPs, with an average particle size of approximately 72.3 nm. To gain further understanding of the core-shell structure and surface properties, a high-resolution TEM image was captured (Figure 1C), which confirmed the presence of a mesoporous silica coating surrounding the Fe_3O_4 core. This observation highlighted the potential of the FS nanoparticles for efficient drug loading and delivery. To further investigate the surface characteristics and porosity of the NPs, N_2 isothermal adsorption and desorption curves were obtained for Fe_3O_4 NPs with or without mesoporous silica layer. It was observed that the specific surface area of the FS nanoparticles increased approximately fourfold after the coating with mesoporous silica, and the average pore size of the FS nanoparticles was measured to be around 6.21 nm (Figure 1D). These findings clearly demonstrated the successful formation of mesoporous silica coating on the surface of the Fe_3O_4 nanoparticles, thereby enhancing their surface area and porosity, which are essential characteristics for an effective nanocarrier in therapeutic agent delivery. Moreover, scanning electron microscopy (SEM) imaging and the corresponding energy-dispersive X-ray spectroscopy (EDS) corroborated the spherical morphology of the FS NPs and confirmed the coexistence of Fe, Si and

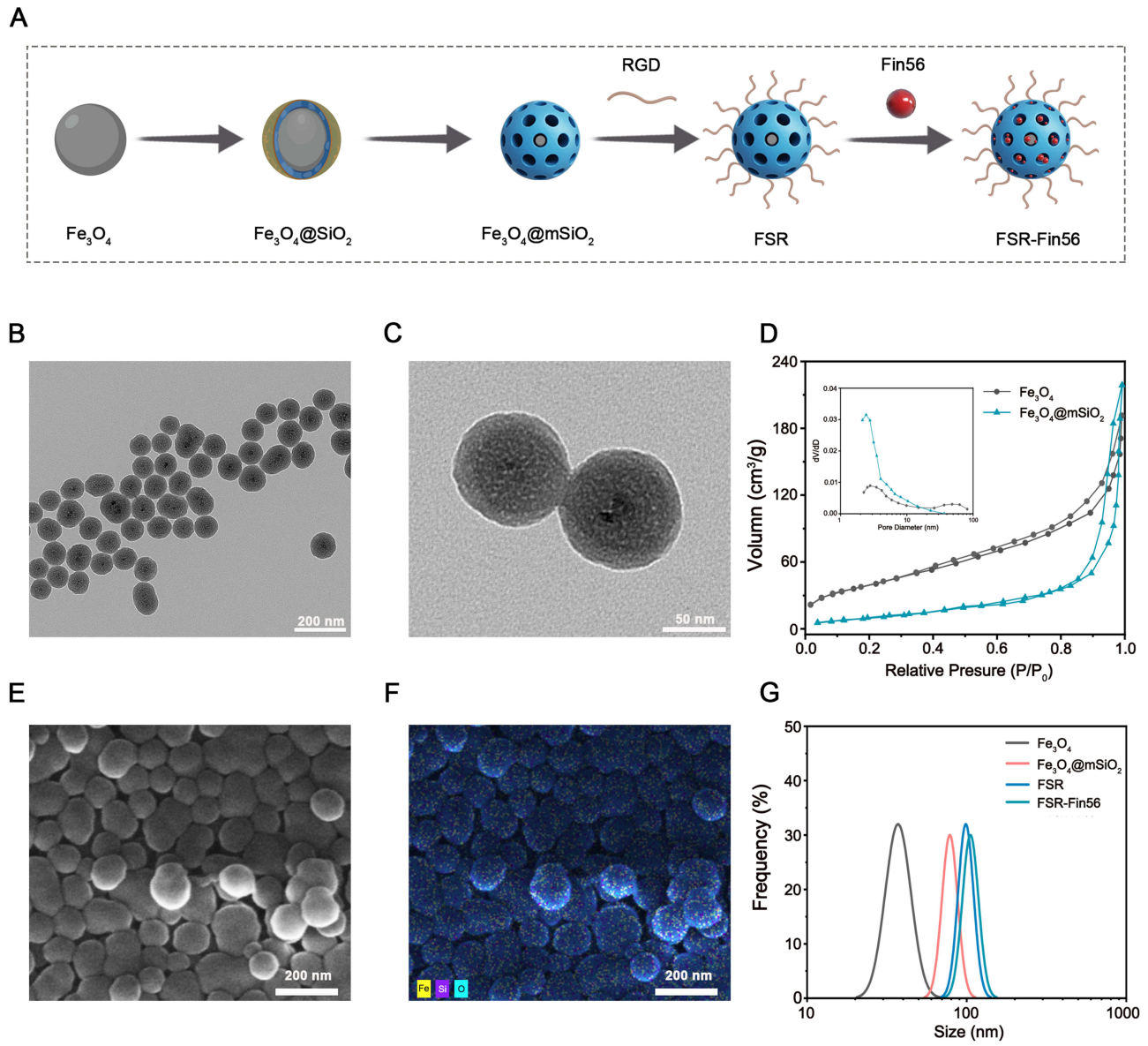

Figure 1 Schematic illustration and characterization of the prepared nanoparticles. (**A**) Schematic illustration of the preparation of FSR-Fin56. TEM images of FS nanoparticles in low resolution (**B**) and high resolution (**C**). (**D**) N2 adsorption/desorption isotherms and pore-size distribution curve (inset) of the Fe3O4 and Fe3O4@mSiO2. SEM image (**E**) of FS nanoparticles and corresponding Elemental mapping (**F**). (**G**) DLS size distribution of Fe3O4, FS, FSR and FSR-Fin56 NPs.

O elements (Figure 1E and F). These comprehensive characterizations collectively demonstrated the compelling suitability of the synthesized FS nanoparticles as an advanced nanocarrier platform for effective drug delivery applications.

The evolution of zeta potential was carefully monitored throughout the synthesis process, revealing distinct changes at each stage. Figure S1A illustrated the zeta potentials of the Fe_3O_4, FS, FSR, and FSR-Fin56 nanoparticles as −19.38±1.46 mV, −34.1±1.73 mV, −24.31±1.74 mV, and −31.76± 1.4 mV, respectively. This stepwise modulation of zeta potential signified the successful assembly of the nanoparticles. Additionally, Fourier-transform infrared (FTIR) spectroscopy was employed to validate the synthesis procedure and assess surface modifications. As demonstrated in Figure S1B, the stretching vibration peak of Si-O-Si at 1085 cm^{-1} confirmed the presence of the silica layer, while the peak at 3300 cm^{-1} corresponded to surface-bound hydroxyl groups, confirming the successful coating of Fe_3O_4 nanoparticles with silica.[33] Notably, the functionalization of RGD peptide led to discernible characteristic peaks of amide I and amide II.[34] These collective findings unequivocally established the successful synthesis of the FSR nanovehicle.

Figure 1G illustrated the hydrated diameters of Fe_3O_4, FS, FSR, and FSR-Fin56 NPs as determined by dynamic light scattering (DLS). The measured diameters were found to be approximately 39.12 nm, 79.91 nm, 100.6 nm, and 107.7 nm, respectively. It was worth noting that the observed increase in size compared to the TEM images could be attributed to the hydration effect of the nanoparticles in the aqueous medium.[35] To evaluate the dispersion and stability of the synthesized nanoparticles, we monitored the dispersity in various media (water, DMEM, and DMEM supplemented with 10% FBS) over a 7-day incubation period. Remarkably, the FSR-Fin56 NPs exhibited excellent dispersity without any noticeable aggregation or precipitation, even after prolonged storage for one week. Notably, the hydrodynamic diameters of the FSR-Fin56 NPs remained relatively unchanged during the entire incubation period in different media, indicating exceptional colloidal stability (Figure S1C). The outstanding dispersity and stability observed in physiological solutions highlighted the promising potential of the FSR-Fin56 nanovehicle for future in vivo applications.

Photothermal Properties

To evaluate the in vitro photothermal properties of FSR NPs, real-time temperature changes of the nanoparticles were monitored using an infrared thermal imaging camera upon near-infrared (NIR) irradiation at 808 nm (Figure 2A). As illustrated in Figure 2B and C, a concentration- and time-dependent increase in temperature was observed for FSR, while the control group (PBS) showed minimal temperature variation. Furthermore, a clear dependence on laser power intensity was observed (Figure 2D). Moreover, the photostability of FSR was rigorously assessed by subjecting the nanoparticles to five cycles of on/off irradiation with an 808 nm laser at 1.0 W cm^{-2} for 5 minutes each. Notably, the temperature variation curves and peak shapes exhibited no noticeable changes (Figure S1D), indicating the exceptional photothermal stability of FSR nanoparticles. Collectively, these compelling results underscored the exceptional photothermal conversion efficiency and remarkable photothermal stability of the as-prepared FSR nanoparticles, positioning them as a highly promising candidate for effective photothermal therapy in the field of cancer treatment.

Hyperthermia-Boosted Fenton Reactivity and GSH Consumption

3,3',5,5'-Tetramethylbenzidine (TMB) was employed to assess the production of hydroxyl radicals (OH·). Upon charge transfer between TMB and OH·, the former acquired two electrons, resulting in the formation of a dimer and a characteristic blue color in the solution, with absorbance at 652 nm (Figure 2E). Notably, in the absence of H_2O_2, which served as the substrate for the Fenton reaction, no significant absorbance was detected (Figure 2F). Encouragingly, the FSR nanoparticles treated with H_2O_2 at pH 5.0 exhibited stronger absorption compared to that at pH 7.4, owing to the enhanced release of iron ions in the tumor microenvironment (TME)-mimicking acidic milieu. Subsequently, the OH·-generation capability under tumor-mimetic high REDOX state was evaluated. Given the well-known inhibitory effect of overexpressed glutathione (GSH) in tumor cells on ROS-based cancer therapies,[36] the FSR nanoparticles were initially reacted with GSH (10 mM) and subsequently treated with H_2O_2 at pH 7.4 or pH 5.0. Significantly, the most prominent absorption was observed in the group treated with GSH and H_2O_2 at pH 5.0, attributed to the heightened Fe^{2+} ions mediated by GSH, thus underscoring the immense potential of the nanoparticles for OH··-generation therapy under TME conditions.

Additionally, to further validate the production of OH·, hydroxyphenyl fluorescein (HPF), which is nonfluorescent in its original form but emits strong fluorescence upon reaction with OH·, was utilized.[37] As shown in Figure 2G, the fluorescence intensity followed a similar trend, confirming the generation of OH· in the reaction system containing GSH and H_2O_2 at pH 5.0. These results provided compelling evidence that the as-prepared FSR nanoparticles possessed exceptional catalytic properties for chemodynamic therapy within the tumor microenvironment, where the higher levels of GSH and acidity effectively activated FSR for enhanced OH· generation.

Furthermore, considering that the catalytic efficiency of the Fenton reaction could be augmented by hyperthermia,[38] we proceeded to evaluate the catalytic performance of FSR NPs at elevated temperatures (Figure 2H). As depicted in Figure 2I, the catalytic activity of FSR NPs exhibited a positive correlation with temperature, and the system demonstrated significantly higher absorbance intensity in the TMB-mediated chromogenic reaction at 50°C, validating the effective achievement of hyperthermia-enhanced CDT. Collectively, the synergistic photothermal and chemodynamic effects could be effectively harnessed by FSR NPs to achieve hyperthermia-boosted CDT within the tumor microenvironment, destroying the REDOX homeostasis for amplified ferroptosis-inducing strategy.

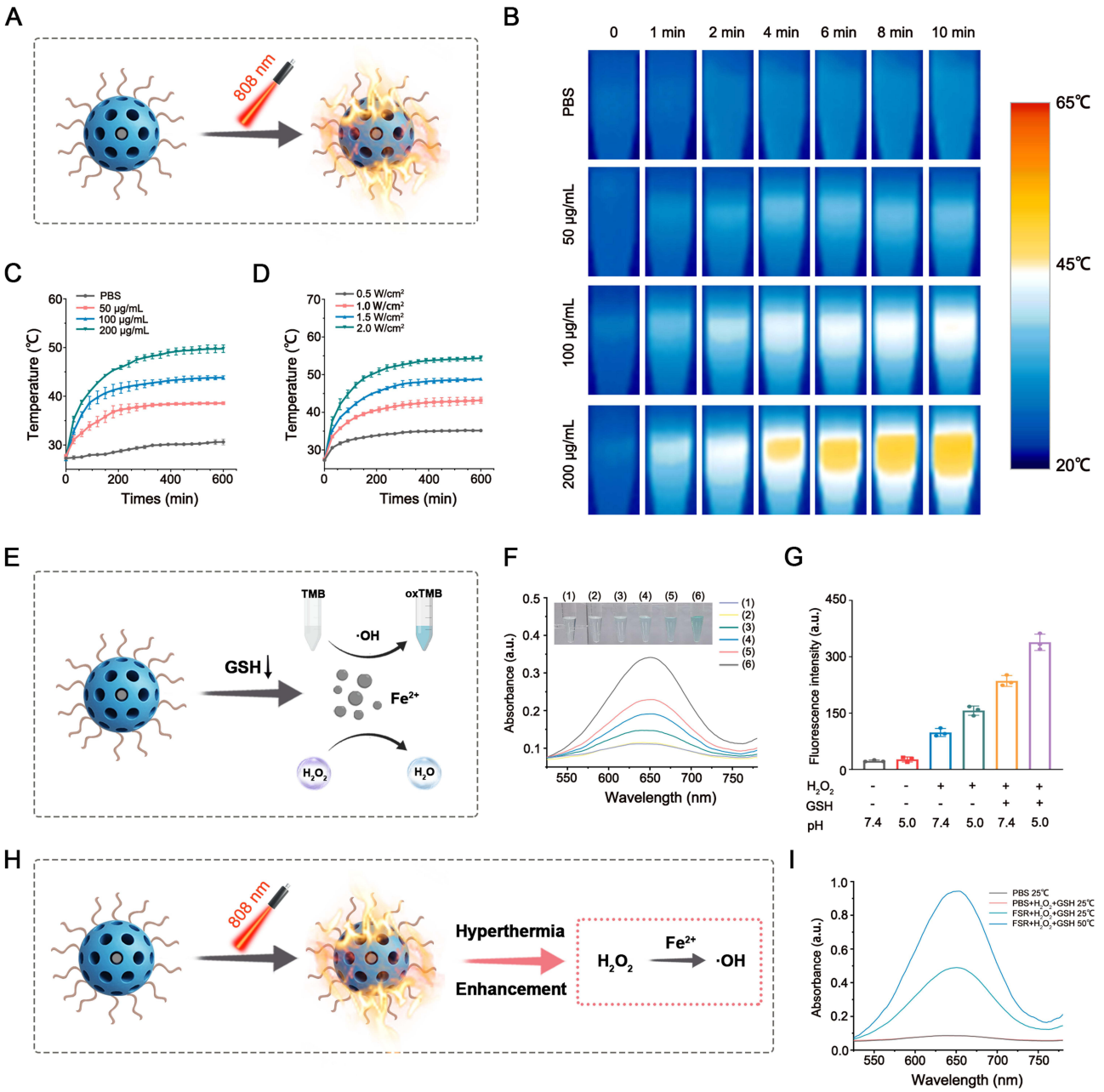

Figure 2 Photothermal and chemodynamic properties of FSR NPs in vitro. (**A**) Illustration of the photothermal effect of FSR. (**B**) The infrared thermal images and time-dependent temperature variety of FSR at different concentrations under 1.0W cm^{-2} NIR laser irradiation. Time-dependent temperature varieties of FSR under 808 nm laser irradiation with different concentrations (**C**) or different power densities (**D**). (**E**) Illustration of the chemodynamic effect of FSR. (**F**) UV-vis spectra and photograph (inset) of TMB solution treated by FSR under different conditions: (1) FSR at pH 7.4; (2) FSR at pH 5.0; (3) FSR plus H_2O_2 at pH 7.4; (4) FSR plus H_2O_2 at pH 5.0; (5) FSR plus H_2O_2 and GSH (10mM) at pH 7.4; (6) FSR plus H_2O_2 and GSH (10mM) at pH 5.0. (**G**) HPF (10μM) fluorescence response after 1h incubation in corresponding reaction systems. (**H**) Illustration of the hyperthermia-boosted chemodynamic effect. (**I**) UV-vis spectra of TMB solution under different treating conditions: (1) PBS under 25°C; (2) PBS plus H_2O_2 and GSH (10mM) under 25°C; (iii) FSR plus H_2O_2 and GSH (10mM) under 25°C; (iv) FSR plus H_2O_2 and GSH (10mM) under 50°C.

Biocompatibility and Drug Delivery

The biocompatibility of nanoparticles is of paramount importance for their potential systemic administration as drug delivery carriers before clinical application.[39] To assess the cytotoxicity of FSR NPs on normal cells, bone marrow-derived mesenchymal stem cells (BMSCs) were subjected to a CCK8 assay. After 72 hours of incubation, no significant cytotoxicity was observed, as evidenced by the cell viability comparable to the control group (Figure 3A). These results underscored the excellent biocompatibility of the FSR NPs, ensuring their safe application as drug carriers. Furthermore, the hemocompatibility of the NPs was evaluated using a hemolysis assay. As depicted in Figure 3B, the positive control

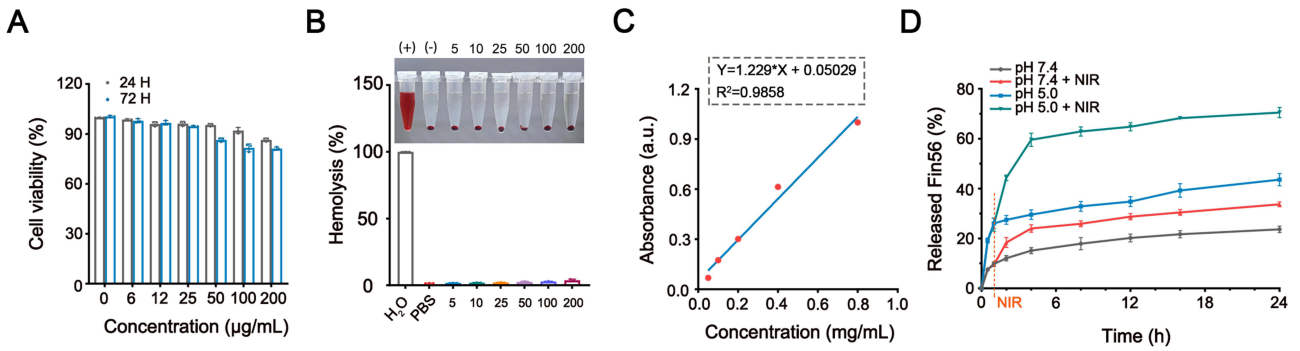

Figure 3 Biocompatibility and release profiles of the nanovehicle in vitro. (**A**) Cell viabilities of BMSCs treated by FSR NPs at a variety of concentrations for 24h and 72h. (**B**) Hemolysis analysis of FSR suspension at various concentrations. (**C**) Standard curve of Fin56 according to the UV-vis absorption. (**D**) The release profiles of Fin56 from FSR-Fin56 in PBS at various pH values with NIR irradiation or not.

group (H_2O) exhibited a distinct red color due to the release of hemoglobin from ruptured red blood cells (RBCs), indicative of hemolysis. In contrast, both the PBS and FSR groups demonstrated negligible hemolysis, confirming the excellent hemocompatibility of the NPs. Collectively, these findings corroborated the outstanding biocompatibility and biosafety of the prepared FSR NPs, rendering them a promising candidate for further exploration in biomedical applications.

Subsequently, FSR was evaluated as a drug delivery system for Fin56 to verify its potential in preventing premature leakage and enabling controlled release. The absorbance of Fin56 at various concentrations was measured, and the standard curve was generated based on the results, as depicted in Figure 3C. Utilizing the standard concentration curve, the loading efficiency of Fin56 in FSR NPs was calculated to be 28.2%. To investigate the TME-responsive release behavior of the NPs, the release profiles of Fin56 under different pH conditions were evaluated. As shown in Figure 3D, a slow release of Fin56 (23.68%) was observed at pH 7.4, whereas at pH 5.5, the amount of released Fin56 increased significantly to 43.57% within the same 24-hour incubation time, indicating a pronounced pH-dependent release behavior. This phenomenon could be attributed to the accelerated decomposition of the Fe_3O_4 core in the acidic TME. Notably, the minimal release of agents at the neutral physiological environment (pH 7.4) suggested that FSR-Fin56 NPs could remain stable and secure for normal tissues.

Furthermore, the NIR-triggered release behavior of the NPs at pH 7.4 or 5.0 was evaluated under 808 nm laser irradiation. As illustrated in Figure 3D, the release of Fin56 was dramatically increased at pH 5.0 after NIR irradiation (1.0 W cm^{-2}) for 10 minutes, resulting in a cumulative release amount of 70.47%. In contrast, the release rates of Fin56 were only slightly increased at pH 7.4 under the same conditions. These findings confirmed that the combination of pH and NIR laser irradiation could serve as an intelligent switch to finely control the release of Fin56 from the nanovehicle, effectively preventing drug leakage and reducing adverse effects on normal tissues.

Cellular Uptake

Efficient and targeted delivery of therapeutic agents to tumors is a critical aspect of nanocomposite-mediated therapies.[40] In order to achieve enhanced internalization into tumor cells, our NPs were designed with RGD functionalization, which has been shown to have an affinity for αvβ3 integrin receptors commonly overexpressed in OS cells.[41] The cellular uptake behavior of the NPs was assessed by co-culturing them with MNNG/HOS cells, and the NPs were labeled with ICG for visualization. After a 6-hour incubation, the intracellular red fluorescence intensity of ICG was evaluated. As depicted in Figure 4A, the cells treated with ICG@FSR NPs exhibited significantly stronger fluorescence signals compared to cells from ICG@FS group, suggesting efficient internalization facilitated by the RGD peptide. For a more visual examination of the uptake behavior, transmission electron microscopy was employed to capture electron micrographs of cells treated with FSR NPs. As shown in Figure 4B, the darker contrast in various regions clearly indicated the substantial accumulation of FSR NPs within the tumor cells. Collectively, these findings demonstrated that the RGD-functionalized nanovehicle could be effectively internalized into tumor cells, offering a promising strategy for targeted delivery of therapeutic agents.

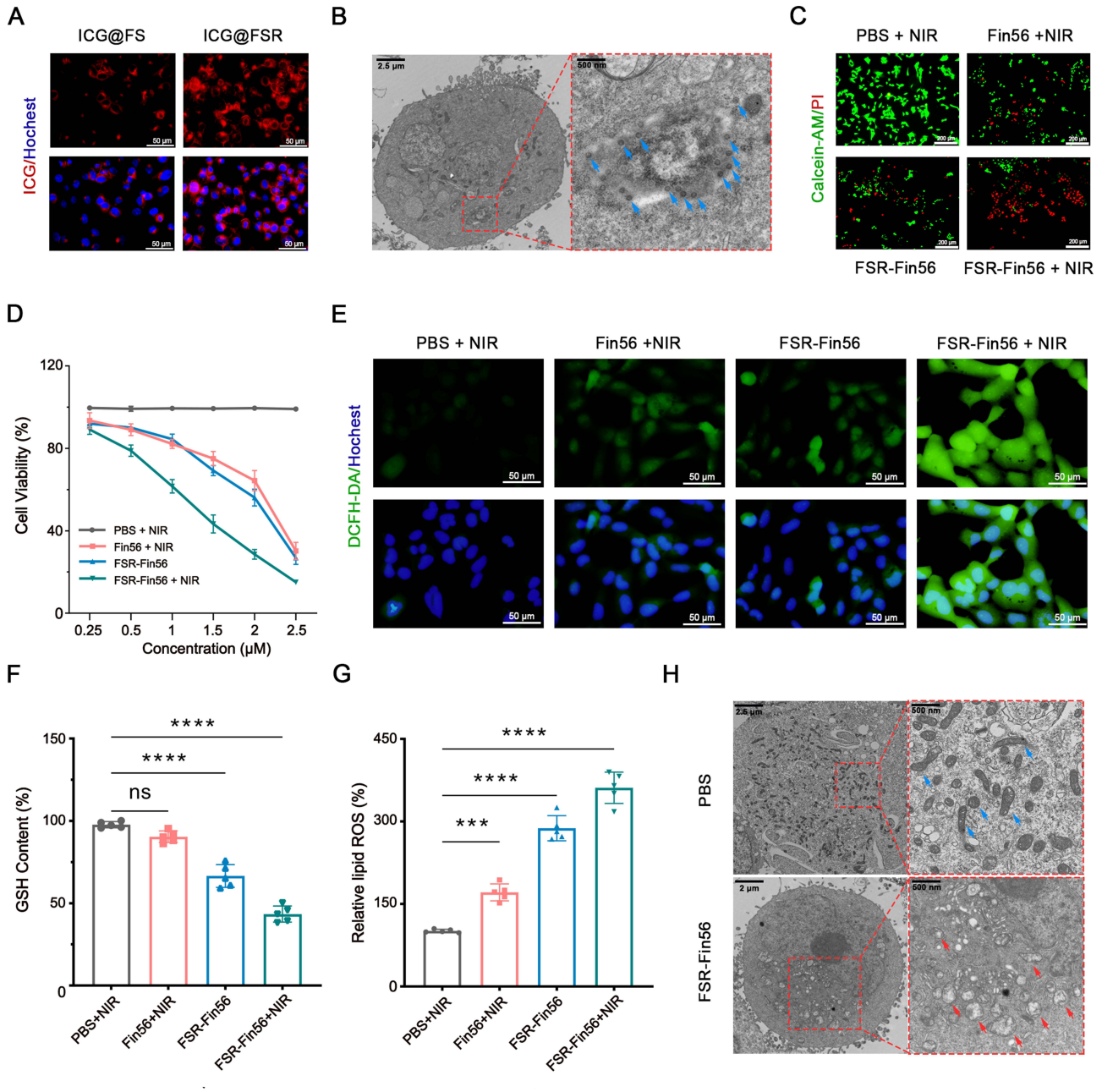

Figure 4 Hyperthermia-boosted chemodynamic effect induced amplified ferroptosis. (**A**) Fluorescence images of MNNG/HOS cells after a 4-hour incubation with ICG@FS or ICG@FSR NPs. (**B**) TEM image of MNNG/HOS cells treated with FSR. The blue arrows indicated the FSR NPs. (**C**) Fluorescence images of MNNG/HOS cells stained with Calcein-AM and PI after different treatments. (**D**) Cell viability of MNNG/HOS cells at 24-hour after corresponding treatments. (**E**) Fluorescence images of MNNG/HOS cells stained with DCFH-DA after various treatments. Relative cellular GSH (**F**) and LPOs (represented by MDA content) (**G**) levels of MNNG/HOS cells after corresponding treatment (***P<0.001, ****sP<0.0001). (**H**) TEM images of MNNG/HOS cells after different treatments. The blue and red arrows indicated relative normal and damaged mitochondria, respectively.

Cellular Cytotoxicity in vitro

Encouraged by the impressive targeting and intracellular accumulation capabilities of the NPs, we proceeded to investigate the synergistic therapeutic effects of this engineered nanovehicle in vitro. We initiated our investigation by conducting the CCK-8 assay to quantify cell viabilities. MNNG/HOS cells were incubated with FSR-Fin56 and other treating agents. As expected, all these formulations exhibited dose-dependent cytotoxicity. Particularly noteworthy was the group treated with FSR-Fin56, which was exposed to NIR light. This group demonstrated the highest rate of cell mortality. This result strongly suggested a synergistic effect between Fin56 and Fe ions when exposed to hyperthermia conditions (Figure 4D).

To visually assess the impact of these treatments on MNNG/HOS cells, we utilized Calcein-AM and PI as fluorescent markers for living (green) and dead (red) cells, respectively. Figure 4C illustrated the outcomes: cells treated with PBS and NIR showed robust vitality, as indicated by the bright and strong green fluorescence. This suggested that mild irradiation without a photothermal agent had minimal cytotoxicity. In sharp contrast, the FSR-Fin56 + NIR group exhibited the most pronounced killing effect, as evidenced by the intense red signals, which corroborated the results obtained from the earlier CCK-8 assay. In summary, these findings conclusively confirmed the outstanding synergistic therapeutic effect of combining CDT/PTT with Fin56, thus amplifying ferroptosis against MNNG/HOS cells.

Amplified Ferroptosis by Hyperthermia-Boosted CDT

As it is widely acknowledged, Fin56 exerts its ferroptosis-inducing effect by promoting GPX4 degradation.[16] GPX4 is recognized as a crucial component in maintaining intracellular redox balance by neutralizing excess ROS and toxic lipid peroxides (LPOs) through the action of glutathione (GSH).[42] Thus, the depletion of GPX4 by Fin56 and the consumption of GSH by FSR are expected to lead to a significant increase in intracellular LPO levels, which serves as a critical hallmark of ferroptosis, ultimately causing irreversible cellular damage.[43] To investigate the underlying mechanism behind the cytotoxic effect mediated by FSR-Fin56 + NIR, we initially assessed the intracellular oxidative stress resulting from the combination of hyperthermia-enhanced CDT and Fin56 treatment. DCFH-DA was used as a fluorescent probe to measure cellular ROS levels. As depicted in Figure 4E, minimal green fluorescence was observed in the control group treated with PBS and NIR, indicating that mild irradiation alone had limited impact on inducing cellular oxidative stress. In contrast, cells treated with Fin56 and NIR or FSR-Fin56 without NIR displayed slight fluorescence, while the FSR-Fin56 + NIR group exhibited the most intense fluorescence, indicating the generation of severe intracellular oxidative stress resulting from the combination of hyperthermia-boosted CDT and amplified ferroptosis.

Subsequently, we examined the intracellular levels of GSH and LPOs. As expected, the FSR-Fin56 + NIR-treated cells showed the lowest GSH levels and the highest accumulation of LPOs (Figure 4F and G), owing to the FSR-induced GSH consumption and the hyperthermia-enhanced production of hydroxyl radicals, which effectively overcame cellular defenses against Fin56-induced ferroptosis. Moreover, transmission electron microscope images of cell sections revealed that mitochondria in cells treated with FSR-Fin56 + NIR exhibited a rounded morphology with disrupted cristae structures (Figure 4H), consistent with the typical characteristics of ferroptosis, as previously reported.[13] Collectively, the combined treatment of Fin56 and FSR successfully disrupted the redox equilibrium in tumor cells, and with the synergistic “turn on” effect of NIR laser irradiation, the cooperative photothermal and chemodynamic therapies achieved a potent and boosted ferroptosis-inducing therapy.

Biodistribution and Photothermal Properties

To explore the in vivo distribution of the nanocomposites in the organism, we intravenously administered ICG-labeled NPs (ICG@FSR) to MNNG/HOS tumor-bearing mice and monitored the fluorescence signals at various time points using an in vivo fluorescence spectrum system. Before injection, no fluorescence signal was detected (Figure 5A). Afterwards, the fluorescence signals in the tumor region gradually increased over time, reaching a peak at 12 hours post-injection, indicating the effective accumulation of NPs within the tumors. Even at 24 hours post-injection, rather strong fluorescence signals could still be observed at the tumor site, demonstrating the excellent retention performance of the NPs. Ex vivo imaging of tumor tissues and major organs (heart, liver, spleen, lung, and kidney) further confirmed the superior intratumoral enrichment capacity of the NPs, as the fluorescence intensity in the tumor tissues remained much stronger than that in the major organs (Figure 5B and C). Additionally, the fluorescence intensity in the liver and kidney areas was relatively noticeable, indicating the potential metabolic clearance pathways of the NPs.[44] These results collectively showcased the effective tumor accumulation and prolonged retention ability of the NPs, which can be attributed to both the RGD-mediated targeting attachment and the enhanced permeability and retention (EPR) effect.[45]

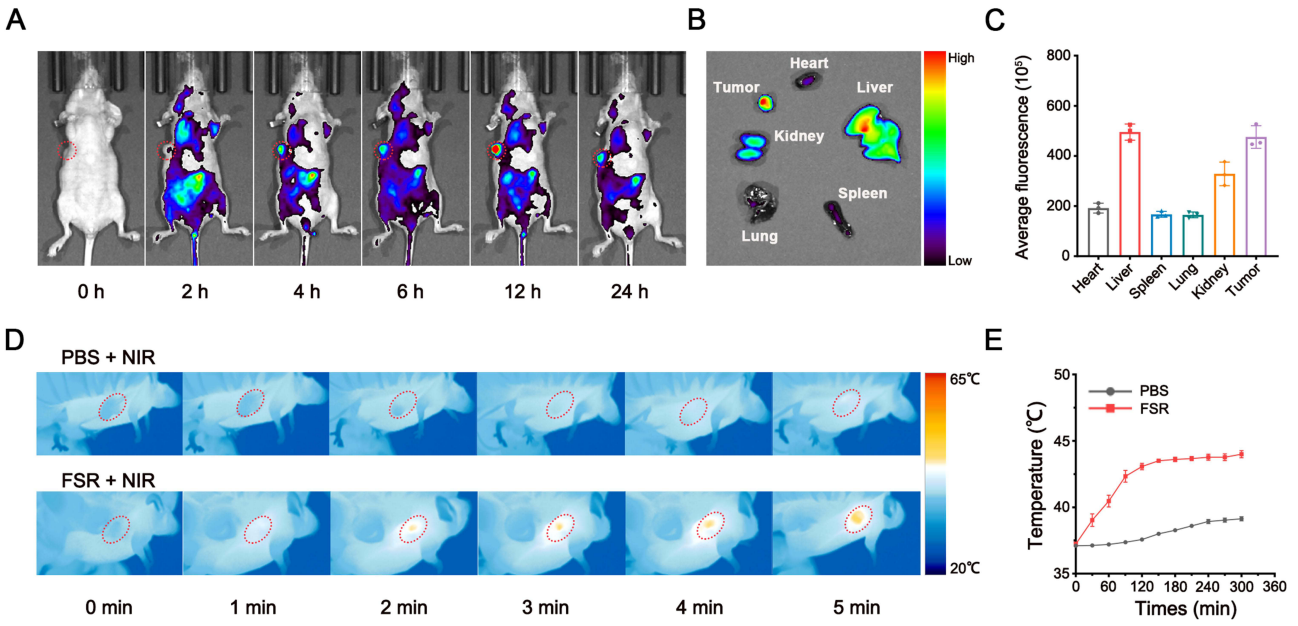

Figure 5 Biodistribution and photothermal effect of FSR NPs in vivo. (**A**) In vivo fluorescence image of MNNG/HOS tumor-bearing mice at various time point after intravenous injection of ICG labeled FSR NPs. (**B**) Fluorescence image of major organs and tumor tissue. (**C**) Semiquantitative analysis of fluorescence intensity in the major organs and tumor tissues. In vivo thermal images (**D**) and temperature variation curves (**E**) of tumor region under NIR laser irradiation (1.0 W cm^{-2}).

According to the in vivo imaging observations, we selected the 12-hour post-injection time point as the optimal time for NIR laser irradiation. As depicted in Figure 5D and E, the temperature in the PBS-treated mice only exhibited a slight increase after exposed to NIR laser irradiation for 5 minutes. In contrast, the temperature at the tumor site in the FSR group reached approximately 45°C under the same conditions, which was favorable for boosting the Fenton catalysis reaction and promoting Fin56 release for amplified ferroptosis. These results underscored the promising photothermal performance of FSR in vivo.

In vivo Antitumor Effect

Motivated by the promising therapeutic effects observed in vitro and exceptional tumor accumulation of the as-prepared NPs, a MNNG/HOS tumor xenograft model was established to further validate the in vivo synergistic therapeutic efficacy of the nanovehicle. The total in vivo treating process is revealed in Figure 6A. As displayed in Figure 6B–D, the tumors of mice treated with PBS and NIR grew rapidly throughout the experiment, indicating that NIR irradiation alone had negligible inhibitory effect on the tumor growth. Meanwhile, the tumors of mice treated with Fin56 + NIR or FSR-Fin56 without NIR were slightly inhibited while the growth of tumors on mice treated with FSR-Fin56 + NIR was noticeably restrained, suggesting the synergistic effect of CDT and PTT for amplified ferroptosis-inducing therapy.

Furthermore, the excellent therapeutic effect was validated by H&E staining of the tumor tissues (Figure 6F), where the most significant death of cells was observed in the FSR-Fin56 + NIR group. Additionally, the expression of Ki-67 was detected by immunofluorescent staining to evaluate the proliferation of tumor cells (Figure 6G). As expected, tumor cells of FSR-Fin56 + NIR treated group exhibited the lowest expression of antigen Ki-67, further confirming the remarkable therapeutic effects of the nanovehicle. Moreover, intratumoral GPX4 level was found significantly down-regulated by FSR-Fin56 (Figure 6H), confirming the NPs successfully initiate a synergistic therapy for boosted ferroptosis-inducing strategy. Of note, among all groups no significant weight loss were detected during the treatment (Figure 6E), indicating negligible systemic toxicity of the NPs. In addition, the levels of ALT and BUN (hepatic and renal function marker) were found to be at normal level, indicating the favorable biosafety of the therapeutic agents (Figure S2). Meanwhile, no obvious histological changes or inflammation lesions were observed on the H&E staining images of major organs (Figure S3). Taken

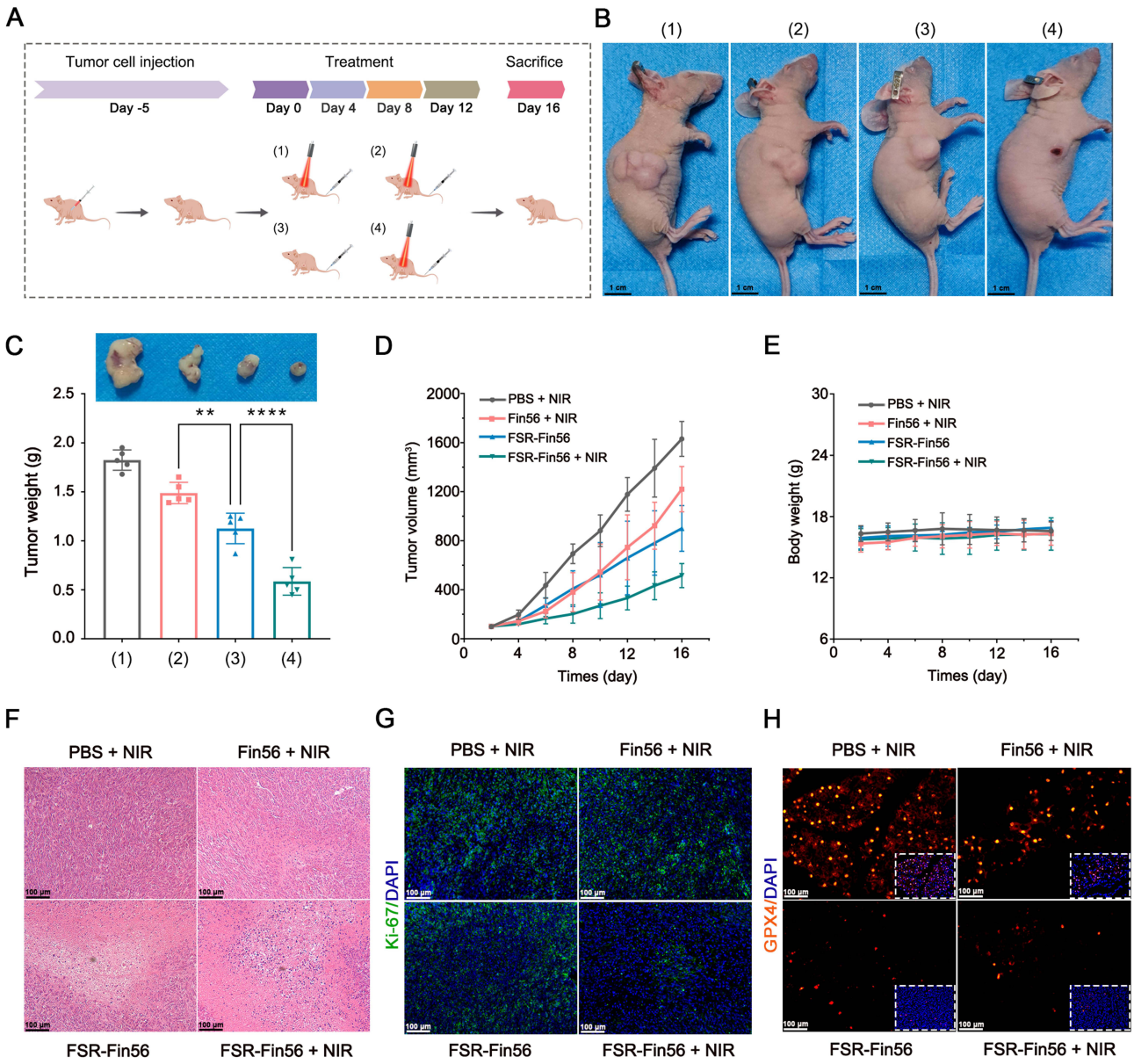

Figure 6 In vivo antitumor effect. (**A**) Illustration of in vivo treating process. (**B**) Representative photographs of the MNNG/HOS tumor-bearing mice after various treatments: (1) PBS + NIR; (2) Fin56 + NIR; (3) FSR-Fin56; and (4) FSR-Fin56 + NIR. (**C**) Average tumor weights and representative photograph (inset) after corresponding treatments: (1) PBS + NIR; (2) Fin56 + NIR; (3) FSR-Fin56; and (4) FSR-Fin56 + NIR (**P<0.01, ****P<0.0001). (**D**) Tumor growth curves of the mice underwent different treatments. (**E**) Body weight curves of the tumor-bearing mice during the treating process. H&E staining (**F**), immunofluorescence staining of Ki-67 (**G**) and GPX4 (**H**) of tumor tissue sections from different groups.

together, these results validated the as-prepared FSR-Fin56 nanovehicle with mild laser irradiation could eradicate tumors effectively without appreciable side effects.

Conclusion

In conclusion, the synthesized biocompatible FSR-Fin56 nanovehicle successfully achieved targeted drug delivery and synergistic therapy by combining hyperthermia-boosted CDT and amplified ferroptosis induction. The in vitro and in vivo results demonstrated its promising therapeutic efficacy and biosafety. This study offered a compelling strategy for cancer treatment, particularly for ferroptosis-sensitive tumors like osteosarcoma.

Acknowledgments

We express our gratitude for the graphical content provided by Figdraw (www.figdraw.com). We acknowledge Ms ZJ. Xiao for her help in figure design. This study was partly supported by the National Natural Science Foundation of China (91949203 and 32130052 to Zhang Y.Z.) and Non-profit Central Research Institute Fund of the Chinese Academy of Medical Science (2019PT320001).

Disclosure

The authors report no conflicts of interest in this work.

References

1. Mirabello L, Zhu B, Koster R, et al. Frequency of pathogenic germline variants in cancer-susceptibility genes in patients with osteosarcoma. *JAMA Oncol*. 2020;6(5):724–734. doi:10.1001/jamaoncol.2020.0197
2. Mintz MB, Sowers R, Brown KM, et al. An expression signature classifies chemotherapy-resistant pediatric osteosarcoma. *Cancer Res*. 2005;65(5):1748–1754. doi:10.1158/0008-5472.CAN-04-2463
3. Dixon SJ, Lemberg KM, Lamprecht MR, et al. Ferroptosis: an iron-dependent form of nonapoptotic cell death. *Cell*. 2012;149(5):1060–1072. doi:10.1016/j.cell.2012.03.042
4. Stockwell BR. Ferroptosis turns 10: emerging mechanisms, physiological functions, and therapeutic applications. *Cell*. 2022;185(14):2401–2421. doi:10.1016/j.cell.2022.06.003
5. Lei G, Zhang Y, Koppula P, et al. The role of ferroptosis in ionizing radiation-induced cell death and tumor suppression. *Cell Res*. 2020;30(2):146–162. doi:10.1038/s41422-019-0263-3
6. Rademaker G, Boumahd Y, Peiffer R, et al. Myoferlin targeting triggers mitophagy and primes ferroptosis in pancreatic cancer cells. *Redox Biol*. 2022;53:102324. doi:10.1016/j.redox.2022.102324
7. Rodriguez R, Schreiber SL, Conrad M. Persister cancer cells: iron addiction and vulnerability to ferroptosis. *Mol Cell*. 2022;82(4):728–740. doi:10.1016/j.molcel.2021.12.001
8. He Y, Liu X, Xing L, Wan X, Chang X, Jiang H. Fenton reaction-independent ferroptosis therapy via glutathione and iron redox couple sequentially triggered lipid peroxide generator. *Biomaterials*. 2020;241:119911. doi:10.1016/j.biomaterials.2020.119911
9. Mu M, Liang X, Zhao N, et al. Boosting ferroptosis and microtubule inhibition for antitumor therapy via a carrier-free supermolecule nanoreactor. *J Pharm Anal*. 2023;13(1):99–109. doi:10.1016/j.jpha.2022.09.003
10. Lv H, Zhen C, Liu J, Shang P. PEITC triggers multiple forms of cell death by GSH-iron-ROS regulation in K7M2 murine osteosarcoma cells. *Acta Pharmacol Sin*. 2020;41(8):1119–1132. doi:10.1038/s41401-020-0376-8
11. Wang Y, Zhang L, Zhao G, et al. Homologous targeting nanoparticles for enhanced PDT against osteosarcoma HOS cells and the related molecular mechanisms. *J Nanobiotechnol*. 2022;20(1):1–28.
12. Fu J, Li T, Yang Y, et al. Activatable nanomedicine for overcoming hypoxia-induced resistance to chemotherapy and inhibiting tumor growth by inducing collaborative apoptosis and ferroptosis in solid tumors. *Biomaterials*. 2021;268:120537. doi:10.1016/j.biomaterials.2020.120537
13. Liu J, Li X, Chen J, et al. Arsenic-loaded biomimetic iron oxide nanoparticles for enhanced ferroptosis-inducing therapy of hepatocellular carcinoma. *ACS Appl Mater Interfaces*. 2023;15(5):6260–6273. doi:10.1021/acsami.2c14962
14. Zhang P, Qiao Y, Zhu L, et al. Nanoprobe based on biominerals in protein corona for dual-modality MR imaging and therapy of tumors. *ACS Nano*. 2023;17(1):184–196. doi:10.1021/acsnano.2c05917
15. Chin Y, Yang L, Hsu F, et al. Iron oxide@chlorophyll clustered nanoparticles eliminate bladder cancer by photodynamic immunotherapy-initiated ferroptosis and immunostimulation. *J Nanobiotechnol*. 2022;20(1). doi:10.1186/s12951-022-01575-7
16. Shimada K, Skouta R, Kaplan A, et al. Global survey of cell death mechanisms reveals metabolic regulation of ferroptosis. *Nat Chem Biol*. 2016;12(7):497–503. doi:10.1038/nchembio.2079
17. Sun Y, Berleth N, Wu W, et al. Fin56-induced ferroptosis is supported by autophagy-mediated GPX4 degradation and functions synergistically with mTOR inhibition to kill bladder cancer cells. *Cell Death Dis*. 2021;12(11):1028. doi:10.1038/s41419-021-04306-2
18. Zhang X, Guo Y, Li H, Han L. FIN56, a novel ferroptosis inducer, triggers lysosomal membrane permeabilization in a TFEB-dependent manner in glioblastoma. *J Cancer*. 2021;12(22):6610–6619. doi:10.7150/jca.58500
19. Mura S, Nicolas J, Couvreur P. Stimuli-responsive nanocarriers for drug delivery. *Nat Mater*. 2013;12(11):991–1003. doi:10.1038/nmat3776
20. Cun J, Pan Y, Zhang Z, et al. Photo-enhanced upcycling H2O2 into hydroxyl radicals by IR780-embedded Fe3O4@MIL-100 for intense nanocatalytic tumor therapy. *Biomaterials*. 2022;287:121687. doi:10.1016/j.biomaterials.2022.121687
21. Xie L, Chen W, Chen Q, et al. Synergistic hydroxyl radical formation, system XC- inhibition and heat shock protein crosslinking tango in ferrotherapy: a prove-of-concept study of "sword and shield" theory. *Mater Today Bio*. 2022;16:100353. doi:10.1016/j.mtbio.2022.100353
22. Qin X, Wu C, Niu D, et al. Peroxisome inspired hybrid enzyme nanogels for chemodynamic and photodynamic therapy. *Nat Commun*. 2021;12(1). doi:10.1038/s41467-021-25561-z
23. Zhang Y, Yang Y, Shi J, Wang L. A multimodal strategy of Fe(3)O(4)@ZIF-8/GOx@MnO(2) hybrid nanozyme via TME modulation for tumor therapy. *Nanoscale*. 2021;13(39):16571–16588. doi:10.1039/D1NR04196G
24. Lin X, He T, Tang R, et al. Biomimetic nanoprobe-augmented triple therapy with photothermal, sonodynamic and checkpoint blockade inhibits tumor growth and metastasis. *J Nanobiotechnol*. 2022;20(1):80. doi:10.1186/s12951-022-01287-y
25. Nicolas-Boluda A, Laurent G, Bazzi R, Roux S, Donnadieu E, Gazeau F. Two step promotion of a hot tumor immune environment by gold decorated iron oxide nanoflowers and light-triggered mild hyperthermia. *Nanoscale*. 2021;13(44):18483–18497. doi:10.1039/D1NR03201A
26. Manivasagan P, Joe A, Han H, et al. Recent advances in multifunctional nanomaterials for photothermal-enhanced Fenton-based chemodynamic tumor therapy. *Mater Today Bio*. 2022;13:100197. doi:10.1016/j.mtbio.2021.100197

27. Laborda E, Puig-Saus C, Rodriguez-García A, et al. A pRb-responsive, RGD-modified, and hyaluronidase-armed canine oncolytic adenovirus for application in veterinary oncology. *Mol Ther*. 2014;22(5):986–998. doi:10.1038/mt.2014.7
28. Fang Z, Sun Y, Xiao H, et al. Targeted osteosarcoma chemotherapy using RGD peptide-installed doxorubicin-loaded biodegradable polymeric micelle. *Biomed Pharmacother*. 2017;85:160–168. doi:10.1016/j.biopha.2016.11.132
29. Yang H, Zhuang Y, Sun Y, et al. Targeted dual-contrast T1- and T2-weighted magnetic resonance imaging of tumors using multifunctional gadolinium-labeled superparamagnetic iron oxide nanoparticles. *Biomaterials*. 2011;32(20):4584–4593. doi:10.1016/j.biomaterials.2011.03.018
30. Wang M, Deng K, Lü W, et al. Rational design of multifunctional Fe@γ-Fe(2) O(3) @H-TiO(2) nanocomposites with enhanced magnetic and photoconversion effects for wide applications: from photocatalysis to imaging-guided photothermal cancer therapy. *Adv Mater* 2018;30(13): e1706747. doi:10.1002/adma.201706747
31. Pan L, Liu J, He Q, Shi J. MSN-mediated sequential vascular-to-cell nuclear-targeted drug delivery for efficient tumor regression. *Adv Mater* 2014;26(39):6742–6748. doi:10.1002/adma.201402752
32. Wu C, Liu Z, Chen Z, et al. A nonferrous ferroptosis-like strategy for antioxidant inhibition-synergized nanocatalytic tumor therapeutics. *Sci Adv*. 2021;7(39):eabj8833. doi:10.1126/sciadv.abj8833
33. Zhu Y, Ikoma T, Hanagata N, Kaskel S. Rattle-type Fe(3)O(4)@SiO(2) hollow mesoporous spheres as carriers for drug delivery. *Small*. 2010;6 (3):471–478. doi:10.1002/smll.200901403
34. Wu M, Zhong C, Zhang Q, et al. pH-responsive delivery vehicle based on RGD-modified polydopamine-paclitaxel-loaded poly (3-hydroxybutyrate-co-3-hydroxyvalerate) nanoparticles for targeted therapy in hepatocellular carcinoma. *J Nanobiotechnol*. 2021;19(1):39. doi:10.1186/s12951-021-00783-x
35. Hu H, Deng X, Song Q, et al. Mitochondria-targeted accumulation of oxygen-irrelevant free radicals for enhanced synergistic low-temperature photothermal and thermodynamic therapy. *J Nanobiotechnol*. 2021;19(1):390. doi:10.1186/s12951-021-01142-6
36. Yang S, Wu Y, Zhong W, Chen R, Wang M, Chen M. GSH/Ph dual activatable crosslinked and fluorinated pei for cancer gene therapy through endogenous iron De-Hijacking and in situ ros amplification. *Adv Mater* 2023;e2304098. doi:10.1002/adma.202304098
37. Lu N, Deng Z, Gao J, Liang C, Xia H, Zhang P. An osmium-peroxo complex for photoactive therapy of hypoxic tumors. *Nat Commun*. 2022;13 (1):2245. doi:10.1038/s41467-022-29969-z
38. Song Q, Zhang Y, Deng X, et al. Amplification of oxidative stress with a hyperthermia-enhanced chemodynamic process and MTH1 inhibition for sequential tumor nanocatalytic therapy. *J Mat Chem B*. 2023;11(17):3836–3850. doi:10.1039/D2TB02673B
39. Lérida-Viso A, Estepa-Fernández A, García-Fernández A, Martí-Centelles V, Martínez-Máñez R. Biosafety of mesoporous silica nanoparticles; towards clinical translation. *Adv Drug Deliv Rev*. 2023;201:115049. doi:10.1016/j.addr.2023.115049
40. Liu F, He T, Gong S, et al. A tumor pH-responsive autocatalytic nanoreactor as a H(2)O(2) and O(2) self-supplying depot for enhanced ROS-based chemo/photodynamic therapy. *Acta Biomater*. 2022;154:510–522. doi:10.1016/j.actbio.2022.10.002
41. Witlox AM, Van Beusechem VW, Molenaar B, et al. Conditionally replicative adenovirus with tropism expanded towards integrins inhibits osteosarcoma tumor growth in vitro and in vivo. *Clin Cancer Res*. 2004;10(1 Pt 1):61–67. doi:10.1158/1078-0432.CCR-0609-03
42. Yang Y, Tian Q, Wu S, et al. Blue light-triggered Fe(2+)-release from monodispersed ferrihydrite nanoparticles for cancer iron therapy. *Biomaterials*. 2021;271:120739. doi:10.1016/j.biomaterials.2021.120739
43. Maiorino M, Conrad M, Ursini F. GPx4, lipid peroxidation, and cell death: discoveries, rediscoveries, and open issues. *Antioxid Redox Signal*. 2018;29(1):61–74. doi:10.1089/ars.2017.7115
44. Ge X, Huang B, Zhang Z, et al. Glucose-functionalized near-infrared Ag(2)Se quantum dots with renal excretion ability for long-term in vivo tumor imaging. *J Mat Chem B*. 2019;7(38):5782–5788. doi:10.1039/C9TB01112A
45. Luo Y, Yang J, Yan Y, et al. RGD-functionalized ultrasmall iron oxide nanoparticles for targeted T_1-weighted MR imaging of gliomas. *Nanoscale*. 2015;7(34):14538–14546. doi:10.1039/C5NR04003E